Lasers in Manufacturing and Materials Processing
https://doi.org/10.1007/s40516-026-00357-5

RESEARCH

Profiling High Powered Laser Beams for Additive Manufacturing by Imaging their Diffuse Reflections

Hao-Yuan Cheng[1] · **David Deisenroth**[2] · **Sergey Mekhontsev**[2] · **Jonathan A. Malen**[1]

Received: 5 March 2026 / Revised: 4 June 2026 / Accepted: 28 June 2026

Abstract
We report a method for profiling high-power laser beams for additive manufacturing (AM) using a monochrome camera to image diffusely scattered light from a rough surface. Conventional laser profiling systems utilized for AM applications can be prohibitively expensive and have limited resolution, limited power tolerance, or can only measure radially symmetric profiles. We compare our diffuse scattering approach to a conventional laser profiler with multiple scattering surfaces (borosilicate crown glass diffuser (Schott N-BK7), Teflon tape, tungsten carbide, and tungsten) over laser spot diameters spanning 80 μm to 1100 μm and powers spanning 100 W to 1000 W for a spot diameter of 98 μm. Spot diameters measured with the N-BK7 glass diffuser had an average absolute difference of 4.1 % across all diameters, relative to a conventional laser profiler. Our method contrasts with conventional laser beam profilers, providing an inexpensive solution for characterizing high-power laser beam profiles in AM applications with common tools in the AM space. As the AM community researches different beam shaping techniques and their effects on melt pool physics, beam profile validation is a key aspect of process planning and monitoring.

Keywords Laser beam profiling · Laser power density distribution · Additive manufacturing · Beam metrology · Diffuse scattering · High-power lasers · Beam shaping · Laser spot size

✉ Jonathan A. Malen
jonmalen@andrew.cmu.edu

[1] Department of Mechanical Engineering, Carnegie Mellon University, Pittsburgh, PA, USA

[2] Engineering Laboratory, National Institute of Standards and Technology, Gaithersburg, MD, USA

Published online: 10 July 2026

Introduction

Laser-based additive manufacturing applications such as laser powder bed fusion (L-PBF) and directed energy deposition (L-DED) rely on high-power laser beams to melt powder and build parts layer by layer. Various conventional shapes for the power density distribution (PDD) have been used, including Gaussian, top hat, and elliptical beams. More recently, different beam shaping approaches including Bessel, ring-shaped (i.e., donut), and dynamic beam shaping have been tested [1–6]. The most widely used PDD is a circular Gaussian beam, and that is the main focus for validating our methodology [3, 7, 8]. An important metric in Gaussian laser beams is diameter, sometimes referred to as “beam width” or “spot size”. Commonly used metrics include $1/e^2$ diameter, which is twice the radial distance where the beam falls to approximately 13.5 % of its peak intensity; D4σ diameter is the diameter where four standard deviations (± 2σ) of the power density distribution are included [9], which is equivalent to the $1/e^2$ diameter for an ideal Gaussian beam. Typical beam diameters for L-PBF range from 50 μm to 500 μm [10, 11]; while L-DED diameters are larger, ranging from 500 μm to 4000 μm [12, 13]. In this study, we will measure and compare the $1/e^2$ diameter from 80 μm to 1100 μm to cover both use cases.

Previous studies have shown that the laser diameter and PDD can strongly influence the properties of finished parts [2, 5, 14]. Large uncertainty in beam diameter or profile can lead to incorrect power density expectations, resulting in either lack of fusion or key-holing during manufacturing, eventually resulting in an inferior or unusable part. Recently, researchers have demonstrated techniques where they intentionally defocus and alter the beam diameter to improve build qualities [15, 16]. Additionally, recent advances in femtosecond welding [17, 18], optical-field-modulated surface structuring [19], and combined-pulse ablation [20, 21] show that laser-processing outcomes depend strongly on the delivered spatial energy distribution. These increasingly complex processes motivate the importance of measuring the correct beam diameter and PDD.

Test methods for laser beam diameter and PDD have been outlined in ISO 11146 and ISO 13694 [9, 22]. Previous approaches to measure the PDD in low-power applications include the knife edge method [23] or directly measuring the beam with a Complementary Metal-Oxide-Semiconductor (CMOS) camera [24, 25]. One uniquely challenging aspect of measuring the laser beam in AM processes is its high power density. At 100 W and 100 μm the peak laser irradiance exceeds 2.5 $\mathrm{MW/cm^2}$, which greatly exceeds the damage threshold of conventional laser beam profilers (approximately 0.03 $\mathrm{mW/cm^2}$) [26]. Commercial beam profilers made for high-power applications use a scanning slit or a beam splitter to sample a very small percentage of the beam [27, 28]. The scanning slit method only measures the 1-dimensional profile of the x and y axes. If the beam lacks circular symmetry or is not near Gaussian in shape, the resulting profile might not precisely represent the actual PDD [29]. One 2-dimensional (2D) measurement method is the spinning disc method, which uses a pinhole to sample the beam, but its resolution can be limited by the pinhole size (20 μm) [30], making it unsuitable to measure beam shapes with small feature sizes. Another method to measure a high-power beam is to pulse the laser with a very low duty cycle (approximately 0.1 %), attenuate the laser further with high optical density (OD) filters in the collimated portion of the beam, and measure the beam directly with a CMOS camera [7]. Nonetheless, measuring the beam diameter at a reduced beam power may not capture thermal effects on the optical train that impact the PDD. Furthermore, some of these approaches can be prohibitively expensive or cannot fit within the spatial constraints of an AM machine. We herein propose a flexible technique capable of imaging a 1000 W, 100 $\mu\mathrm{m}$ Gaussian beam (approximately 25 $\mathrm{MW/cm^2}$ at the center) at 100 % duty cycle using a monochrome camera to image diffusely scattered laser radiation to find both the beam diameter and PDD. This method has resolution comparable to CMOS based laser beam profilers and is capable of measuring arbitrary beam shapes.

Methods

Camera and Machine Setup

We used the Fundamentals of Laser-Matter Interaction (FLaMI) testbed at the National Institute of Standards and Technology (NIST) to validate our profiling method [31]. The FLaMI testbed is equipped with a Yb-doped fiber laser (1070 nm) with a maximum output power of 1 kW. The estimated standard uncertainty of the power is ± 2.5 %. The laser has been previously calibrated at different powers, with less than 1 % difference in beam diameter between 1 mW, 100 W and 1 kW powers. A gantry installed with a precision laser distance finder (KEYENCE LK-G32[1]) with a maximum error of ± 2.5 $\mu\mathrm{m}$ was used to determine the distance of the test material from the exit aperture of the laser optical train.

The "ground truth" laser beam diameter and profile were measured with the Edmund Optics Beam Profiler 4M [26]. Measurements were performed at < 1 mW of thermal load on the optics, directly imaging the laser beam onto the CMOS windowless focal plane array (WFPA). The use of WFPA eliminates any assumptions about the refractive index and window glass thickness, which change the optical path distance to the sensor. The laser was set to 100 W and pulsed at durations of 100 $\mu\mathrm{s}$ at 5 Hz (0.05 % duty cycle) while synchronously triggering the beam profiler. Past research has shown that the beam diameter measured at low power, low duty cycle is representative of the beam under high-power continuous operations [31]. The laser was attenuated with neutral density (ND) filters with attenuation of approximately 1×10^{10} to avoid damaging the beam profiler. The beam profiler has a pixel pitch of 5.5 $\mu\mathrm{m}$ and the images are fitted with a 2D Gaussian distribution to find the $1/e^2$ beam diameter.

The Photron FASTCAM Mini AX200 high-speed monochrome camera was set up to capture the diffuse scattering of the laser. The AX200 is paired with the Infinity K2 DistaMax lens, a standard (STD) objective lens and two lens extenders (NTX

[1] Certain equipment, instruments, software, or materials, commercial or non-commercial, are identified in this paper in order to specify the experimental procedure adequately. Such identification does not imply recommendation or endorsement of any product or service by NIST, nor does it imply that the materials or equipment identified are necessarily the best available for the purpose.

2× Tube). Any camera can be used as long as a well defined homography method is in place to convert images to real space dimensions. The camera was set to capture RAW images such that the linear relationship between light input and pixel values is not corrupted by the camera's image signal processor (ISP) or settings such as white balance or gamma. The aperture was set to its most open position to minimize diffraction effects from the aperture, which become more significant at longer wavelengths. The diffraction-limited Airy disk diameter can be estimated by $d = 2.44\lambda N$, where λ is the wavelength and N is the aperture *f*-number. For example, the Airy disk size at 1070 nm at *f*/2.8 is 7.3 μm, and 83.6 μm at *f*/32. Thus a larger aperture should be used to achieve higher resolution. Other more cost-effective camera and lens combinations such as a commercial FLIR monochrome camera (BFS-U3-04S2M) with a Computar varifocal zoom lens (MLH-10X) have also been tested on the Trumpf TruLaser Cell 3000 L-DED machine equipped with the Trudisk 6001 laser (1030 nm) and a 3-beam nozzle (SO12) at Carnegie Mellon University (CMU). The specifications of the AX200 camera are shown in Table 1. The AX200 is mounted horizontally on the top side of the test chamber, a mirror is used to view the laser spot as shown in Fig. 1. The AX200 and mirror were placed so that the camera viewed the surface plane at

Table 1 FASTCAM Mini AX200 camera specifications

Specification	FASTCAM Mini AX200
Pixel Size (μm)	20
Resolution	1024 pixels × 1024 pixels
Maximum Frame Rate (FPS)	10 800 at 768 pixels × 768 pixels
Bit Depth (bit)	12

*Measurements were acquired at 1000 fps for laser beam diameters larger than 100 μm, and at 10000 fps for the 80 μm and 100 μm cases

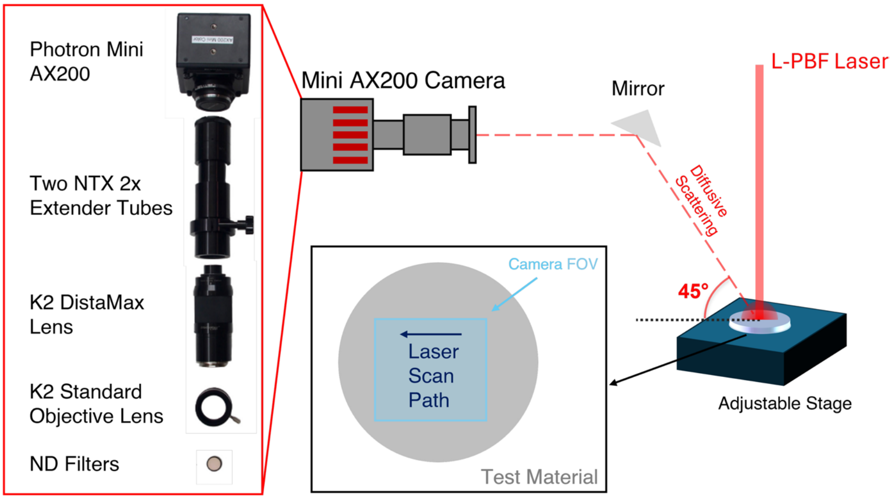

Fig. 1 The AX200 high-speed camera with variable zoom lens and ND filters mounted inside the FLaMI testbed. The camera images the diffuse scattering of the laser scanning a track on a test material through a mirror

an effective imaging angle of 45°. The working distance of the camera is measured at 180 mm ± 5 mm. Depending on the power and spot diameter, the attenuation used was in the range of approximately $1 \times 10^{0.5}$ to $1 \times 10^{2.0}$. Several diffuse surfaces were tested to find the best candidate in Section "Material Selection". A photo of the actual setup is shown in the Appendix (See SI.3).

The laser was scanned in lines of 5.6 mm in length for each power, velocity, and spot diameter. Motion blur was negligible for the microsecond integration times used here. We focused the camera on the laser beam and scanned along the axis of the intersection of the image plane and target plane, keeping the beam in focus while scanning. The laser spot diameter was varied between 80 μm and 1100 μm by adjusting the distance of the diffuse surface relative to the focal plane of the laser. The power was varied between 100 W and 1000 W, as shown in Table 2.

The camera's pixel scale and perspective correction were calibrated at the laser wavelength using a checkerboard pattern calibration target (Edmund Optics 12-202) [32]. The opal checkerboard target has a pattern size of 1.4 mm $\times$ 1.4 mm ± 0.005 mm. A lens was placed in front of the 1070 nm fiber laser to heavily defocus the beam and illuminate the target. The focus was then manually adjusted so that the camera was focused at the 1070 nm wavelength, eliminating any achromatic effects from the camera lens (e.g., that may result from focusing the lens based on visible wavelengths). A homography transformation and scale calibration were performed prior to each experiment. (See SI.1)

Material Selection

The choice of a suitable diffuse reflecting surface is essential for reliable beam profiling with our methodology. We aimed to identify materials that could diffusely scatter an incident laser beam while withstanding the high laser power under operational conditions. Five candidate materials were evaluated for their optical scattering properties, reflectance characteristics, and damage threshold. The tested surfaces include polytetrafluoroethylene (PTFE) tape, N-BK7 glass diffusers, surface-roughened fused silica, and electrically discharge-machined (EDM) tungsten (W) and tungsten carbide (WC). The PTFE tape was from DuPont, MIL-T-27730A compliant, the N-BK7 glass diffusers were acquired from Thorlabs (DG20-1500), surface-roughened fused silica was ground in-house at NIST, W and WC were sourced from McMaster-Carr and EDM-machined at CMU. While the PTFE showed both volumetric and surface scattering, the scattering effects on other materials were mainly on the surface [33]. Below, we provide a detailed description and comparative evaluation of each material. The surface roughness of PTFE tape was measured by atomic force microscopy (AFM) over an area of 50 μm by 50 μm, while the surface roughnesses of WC, W were measured with a Keyence VR-6200 optical profilometer over a 3 mm by 3 mm area. The surface roughness of N-BK7 glass diffuser was measured using a Mitutoyo SJ-210 surface roughness tester. The surface roughness of the 400-grit fused silica

Table 2 FLaMI testbed parameters

Power (W)	100 to 1000
$1/e^2$ Laser beam diameter (μm)	80 to 1100
Scan length (mm)	5.6

was linearly interpolated based on surface roughness measurements of 220-grit and 600-grit fused silica measured with the Mitutoyo SJ-210 surface roughness tester. The surface roughness of each material is shown in Table 3.

Polytetrafluoroethylene (PTFE) is well known for its high reflectance and excellent diffuse scattering properties. Due to its characteristics of being a nearly diffuse reflector, PTFE has been used as a diffuse-reflectance standard in the spectral range from 200 nm to 2500 nm by NIST [40]. An 80 μm thick layer of PTFE tape was stretched across an aluminum block with a hollow center so that the laser impinged directly on the tape without any underlying substrate as shown in Fig. 3a. Advantages of using PTFE tape include its smooth surface, and constant reflective properties with respect to temperature (< 0.05 % change per kelvin) [41], ensuring that image quality remains unaffected by changes in temperature [42, 43]. However, its low melting point (600 K) limits the range of measurable powers. In addition, volumetric scattering [33] inside the PTFE tape can lead to a slight overestimation of the laser spot size under imaging.

N-BK7 is a borosilicate crown glass frequently used in optical components due to its high transmission in the visible to near-infrared range. We employed a surface-engineered diffuser from Thorlabs (DG20-1500), which was ground to a 1500-grit finish, with a RMS surface roughness of 0.20 μm. N-BK7 exhibits a high transmission of approximately 88 % (i.e., low absorption) at 1070 nm [44], a glass transformation temperature of 830 K [45], and an extremely low bulk scattering coefficient [46]. The sample produced uniform, stable diffuse reflections and showed no visible damage at high laser powers (1000 W, 100 μm, 100 % duty cycle, 0.1 s). The N-BK7 diffuser was positioned with its grit-polished surface facing the incoming laser, ensuring that the camera observed the diffuse surface directly. A homemade glass diffuser was also tested; Fused silica (i.e., amorphous SiO_2) plates were roughened using 400-grit sandpaper to enhance diffuse surface scattering. Fused silica also has high transmission at 1070 nm, and a high glass transformation temperature of 1480 K.

Two tungsten-based materials were also evaluated: EDM-processed WC and W. EDM-processed WC has a matte metallic finish with an RMS surface roughness of approximately 0.98 μm. WC exhibits high hardness, and a high melting point of

Table 3 Measured root mean square (RMS) surface roughness, melting / transformation temperature, and room temperature reflectivity at 1070 nm of tested diffuse materials

Material	RMS Roughness (μm)	Melting / Transformation Temp. (K)	Reflectivity
PTFE	0.23	600	0.99 [34, 35]
N-BK7-1500	0.20	830	$< 0.12^{*}$
Fused Silica (400-grit)	$1.30^{\dagger}$	1480	$< 0.17^{\ddagger}$
WC	0.98	3143	0.41 [36]
W	1.52	3695	0.60 [37]

* Based on room temperature transmission of 0.88 [38]

† Interpolated based on surface roughness of 220-grit and 600-grit fused silica since the original sample is no longer available

‡ Based on room temperature transmission of 0.83 (interpolated with 220-grit and 600-grit fused silica) [39]

3143 K. The W sample underwent the same EDM process, yielding a RMS roughness of 1.52 μm. Tungsten has an exceptionally high melting point of 3695 K and high thermal conductivity, enabling it to tolerate high-power lasers. However, high absorption of the laser power in opaque materials heats up the sample and introduces thermal emission, which may skew the measured PDD. Furthermore, temperature-dependent emissivities for both materials may skew the perceived laser beam shape. For example, W has a reflectivity of 0.60 at 1000 K and a higher reflectivity of 0.65 at 2600 K [37], which may change the apparent diffuse scattering profile of the laser beam. Band pass filters with narrow passbands at the laser wavelength can be used as an additional precaution to reduce the competing signal due to broadband thermal emission.

Data Processing and Uncertainties

The RAW videos were captured with a resolution of 12-bit (integral digital levels from 0 to 4095 for each pixel). Each frame in the video was processed using a centroid tracking approach. The homography transformation was first applied to the RAW images to correct for camera perspective, then a threshold at 150 digital levels (approximately 3.7 %) was applied to exclude pixels with low signal to noise ratios. A binary image was generated, as shown in Fig. 2a. The centroid is then calculated from the mean location of all the white pixels and a region of interest (ROI). The ROI, which ranges from 10 pixels $\times$ 10 pixels to 90 pixels $\times$ 90 pixels based on spot diameter, is cropped from the original grayscale image. Finally, we average all the cropped frames (approximately 100 frames) to even out speckles resulting from surface roughness, and the resulting grayscale image (Fig. 2b) is used to determine the profile. The resulting signal is assumed to be proportional to incident laser power, and the CMOS sensor response linearity was evaluated and is assumed to have a negligible effect (estimated ± 1.5 %, see SI.2) on measured

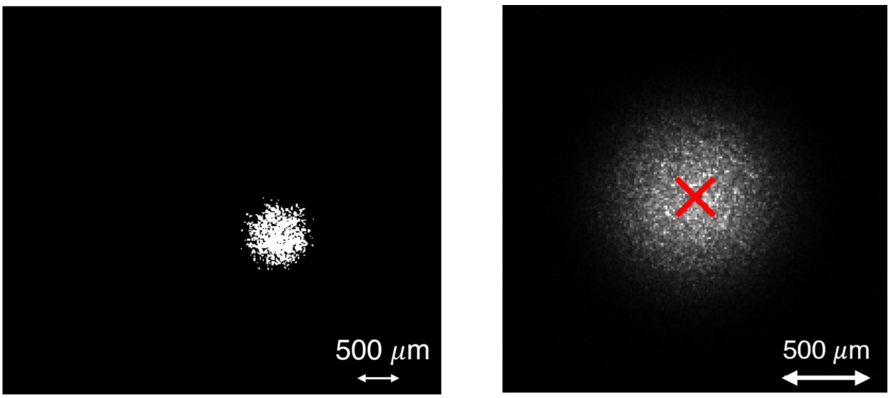

(a) (b)

Fig. 2 (**a**) Binary image of laser spot after homography correction (**b**) 90 pixels $\times$ 90 pixels region grayscale image of the laser spot. The red cross denotes the calculated centroid from (a) beam diameter. A 2D-Gaussian distribution was used (Eq. 1) to determine the $1/e^2$ diameter. Naturally, non-Gaussian beam shapes would require different evaluation of the 2D PDD data.

The fitted 2D-Gaussian distribution is defined as

$$S = A * \exp\left(-\left[\frac{2\left(x_{\mathrm{j,rot}} - x_0^{\mathrm{rot}}\right)^2}{w_{x,rot}^2} + \frac{2\left(y_{\mathrm{j,rot}} - y_0^{\mathrm{rot}}\right)^2}{w_{y,rot}^2}\right]\right) \tag{1}$$

where j is the pixel index and

$$x_{\mathrm{j,rot}} = x_{\mathrm{j}}\cos(\theta) - y_{\mathrm{j}}\sin(\theta), \qquad y_{\mathrm{j,rot}} = x_{\mathrm{j}}\sin(\theta) + y_{\mathrm{j}}\cos(\theta) \tag{2}$$

$$x_0^{\mathrm{rot}} = x_0\cos(\theta) - y_0\sin(\theta), \qquad y_0^{\mathrm{rot}} = x_0\sin(\theta) + y_0\cos(\theta) \tag{3}$$

and

- S is the camera signal digital level at pixel j,
- A is the amplitude,
- $w_{x,rot}$ and $w_{y,rot}$ are half the $1/e^2$ diameter in the rotated x- and y-directions,
- x_0 and y_0 are the centroid positions previously calculated,
- θ adjusts for the rotation of the beam.

We then use a nonlinear least-squares solver to fit $A, w_{x,rot}, w_{y,rot}, \theta$ to determine the major and minor axes of the 2D laser profile over all of the pixels in the ROI. The resulting fitting domain ranges from approximately 100 pixels for a 100 μm beam to 10,000 pixels for a 1000 μm beam.

The uncertainties in the fitted diameters were estimated using the approach outlined by Deisenroth et al. [7]. The factors contributing to uncertainty include: deviation from a circular profile ($u_{circular}$), quantified as the root-mean-square error (RMSE) of the measured beam radius relative to an equivalent-area circle; pixelation and noise ($u_{pixelation}$, approximately 0.07 %), which accounts for errors due to discrete sampling and sensor noise, particularly significant when the beam diameter approaches $10\times$ the pixel pitch; curve fit error (u_{fit}), calculated by dividing the RMSE of the fit residuals by the local slope of the beam intensity profile; measurement repeatability (u_{tests}), defined as the standard deviation of repeated observations; vertical misalignment of the sensor relative to the build plane ($u_{vertical}$, approximately 0.7 %); and sensor non-linearity ($u_{nonlinear}$, approximately 1.5 %, see Appendix SI.2). The total uncertainty can be calculated as the root sum of squares of these components:

$$u_{total} = \sqrt{u_{circ}^2 + u_{pix}^2 + u_{fit}^2 + u_{tests}^2 + u_{vert}^2 + u_{nl}^2} \tag{4}$$

See SI.4 for detailed results quantifying the uncertainty from each component.

Results

The averaged frames of the diffusely scattered laser beam and the measured diameters on different materials are shown in Fig. 3 for a laser power of 100 W and a raster speed at 50 mm/s. The laser profiler “ground truth” $1/e^2$ diameter is 1030 μm. Both PTFE tape and N-BK7 glass diffuser showed smooth, Gaussian-like profiles, while WC showed clear streaks that result from EDM marks. The results on fused silica and N-BK7 match closest to the profile measured by the laser profiler, and only the N-BK7 is within the computed uncertainty. The results show that while PTFE had a much smoother surface compared to fused silica, volumetric scattering inside the PTFE tape can lead to overestimation of the spot diameter.

By moving the scattering surface upward in the beam caustic of the laser on the FLaMI testbed, we tested beam diameters in both L-PBF (approximately 100 μm) and L-DED (approximately 1000 μm) processing regimes. The measured $1/e^2$ diameters based on diffuse scattering at a power of 100 W on both the N-BK7 glass diffuser and the PTFE are shown in Fig. 4a. The measured diameters closely match the diameter measured by the Edmund Optics Beam Profiler 4M. The error bars represent the total uncertainties (Eq. 4) for each material.

The PDDs along the x-axis for both 1000 μm and 80 μm are compared to the beam profiler distributions in Fig. 4b and c. The distribution at 1000 μm is more of a cone shape than a Gaussian beam because measurements were taken far from the focal plane of the laser. Both distributions measured by diffuse scattering closely match the distributions measured by the beam profiler, with root mean-squared errors of the x-data in Fig. 4 of 4.9 % at 1000 μm and 2.6 % at 80 μm.

Figure 5 shows the difference in the measured diameter between the diffuse scattering and the beam profiler. Spot diameters measured with the N-BK7 glass diffused had an average absolute difference of 4.1 % across all diameters, relative to a conventional laser profiler.

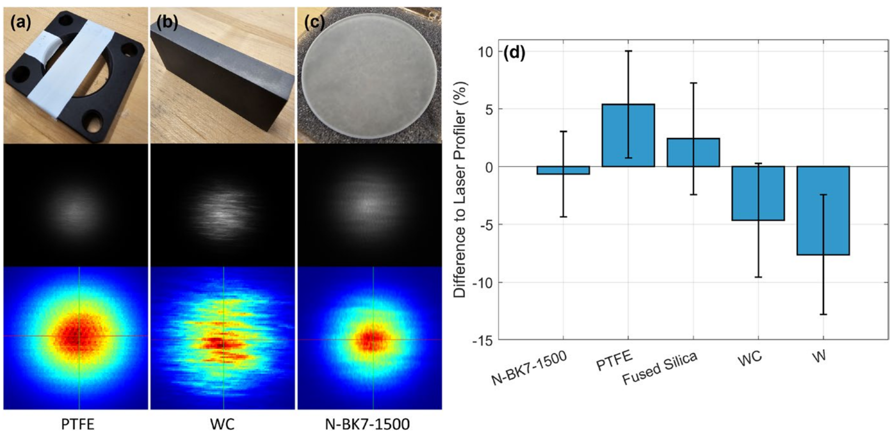

Fig. 3 (**a**)(**b**)(**c**) From top to bottom: image of material, averaged stacked frames RAW image, contour of the averaged stacked frames. (**d**) Difference of measured diameter compared to a beam profiler for different materials

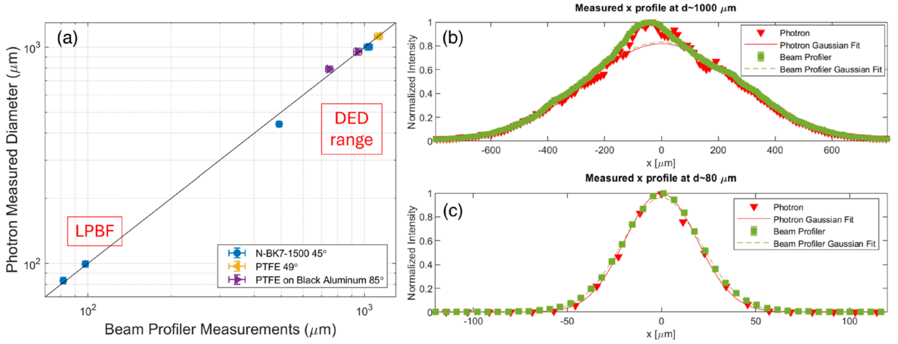

Fig. 4 (**a**) Measured diameter compared to beam profiler measurements for N-BK7, PTFE, and PTFE taped to black anodized aluminum at different effective imaging angles from horizontal. (**b**) Profile of 1000 μm beam on N-BK7 along the x-axis compared to a beam profiler. (**c**) Profile of 80 μm beam on N-BK7 along the x-axis compared to a beam profiler

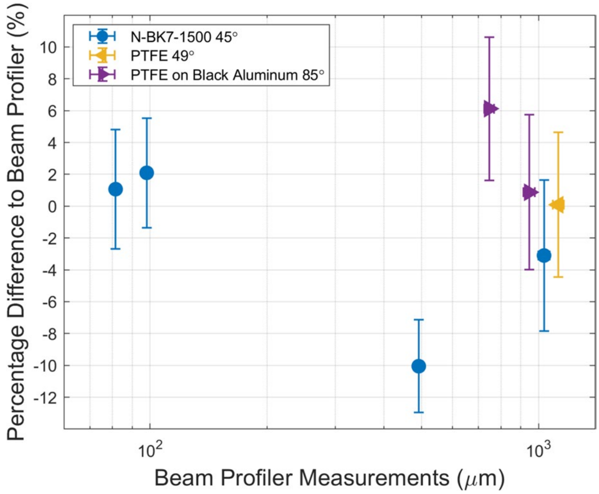

Fig. 5 Difference in diameter compared to beam profilers

Discussion

Effect of Power and Camera Placement

Four different powers ranging from 100 W to 1000 W at a diameter of 98 μm were tested on the FLaMI testbed to evaluate if thermal expansion of the N-BK7 diffuser under high power densities would affect the measured spot diameter. The results in Fig. 6a show that the measured spot diameter differs by at most 4 %, which agrees with prior measurements of power-independent spot diameter on the FLaMI testbed [31]. Furthermore, the maximum strain induced by a Gaussian heat source was calculated assuming that the glass diffuser reaches transformation temperature (830 K) [45]. The strain in the z-direction at the laser center is estimated to be 0.14 %,

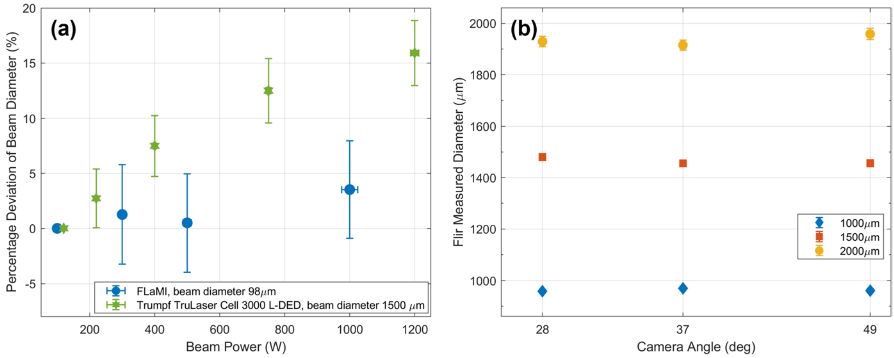

Fig. 6 (**a**) Percentage deviation of beam diameter compared to the diameter at minimum power for FLaMI testbed (100 W) and TruLaser Cell 3000 (120 W). The imaging angle was 45° for the FLaMI testbed and 49° for the TruLaser Cell 3000. (**b**) Measured TruLaser Cell 3000 beam diameter at 120 W for camera imaging angles at 28, 37, 49 degrees to horizontal

which results in 2.8 μm height difference on the 2 mm thick N-BK7 glass diffusers therefore not significantly affecting the focal plane of the laser or camera [47]. In contrast, the same measurements were conducted on the Trumpf TruLaser Cell 3000 L-DED machine at CMU with the beam diameter set at 1500 μm and an imaging angle of 49°. The results in Fig. 6a show that there is a 15.9 % increase in beam diameter at 1200 W compared to the measured beam diameter at a minimum power of 120 W. This proves that in some laser systems the spot diameter may be a function of laser power, which is a potentially important consideration for evaluating and characterizing machine performance. Our diffuse scattering approach is capable of measuring high powers without attenuation or low duty cycle for durations typical of AM builds.

Different effective imaging angles were tested with a FLIR monochrome (BFS-U3-04S2M) camera [48] imaging diffuse laser scattering from CMU's Trumpf TruLaser Cell 3000 L-DED machine with the power set to 120 W. As shown in Fig. 6b, measurements at different angles show consistent spot diameters, which allows for some flexibility in camera placement in spatially constrained environments.

Limitations

The resolution of profile measurement is ultimately limited by the optical resolution of our camera and lens. The optical resolution of the K2 DistaMax zoom lens when using the STD objective lens at a working distance of 370 mm is 6.5 μm [49]. The Airy disk diameter at a wavelength of 1070 nm with an aperture of *f*/2.8 is 7.3 μm, which indicates that we are close to the theoretical optical limits of the method. ISO 11146 and ISO 13694 [9, 22] recommend having at least 10 pixels within the beam diameter for measurements. Therefore, according to this standard, the minimum spot diameter that can be measured by diffuse scattering with this specific optical setup is 70 μm to 80 μm.

Conclusion

We present a laser beam measurement technique capable of measuring high-powered laser beams used in additive manufacturing processes using an off-the-shelf monochrome camera and a N-BK7 glass diffuser. Multiple materials were tested as the scattering surface and the N-BK7 achieved the best agreement with a commercial beam profiler. Spot diameters measured with the N-BK7 glass diffuser had an average absolute difference of 4.1 % across all diameters, relative to a conventional laser profiler. This method also mitigates the need for specialized equipment, giving researchers and industry professionals the capability to validate machine laser beam profiles and diameters of arbitrary beam shapes with existing tools in the AM space. Laser beam PDD measurements assist validation and understanding of beam shape/profile and melt pool physics for further research in beam shaping, process monitoring, and manufacturing machine qualification.

Supplementary Information The online version contains supplementary material available at https://doi.org/10.1007/s40516-026-00357-5.

Acknowledgements A portion of this research was sponsored by the Army Research Laboratory, United States and was accomplished under Cooperative Agreement Number W911NF-20-2-0175. The views and conclusions contained in this document are those of the authors and should not be interpreted as representing the official policies, either expressed or implied, of the Army Research Laboratory or the U.S. Government. The U.S. Government is authorized to reproduce and distribute reprints for Government purposes notwithstanding any copyright notation herein. This work was also supported by Army ERDC Grant No. 1990749. The author acknowledges the use of the NextManufacturing facilities at Carnegie Mellon University.

Author Contributions H.Y.C.: Writing - original draft, Conceptualization, Methodology, Software, Validation, Formal analysis, Investigation, Data Curation, Visualization. D.D.: Writing – review & editing, Methodology, Investigation, Resources, Data Curation, Conceptualization, Supervision. S.M.: Methodology, Investigation, Resources, Conceptualization. J.M.: Writing – review & editing, Supervision, Resources, Methodology, Funding acquisition, Conceptualization, Visualization.

Funding Open Access funding provided by Carnegie Mellon University. This research was sponsored by the Army Research Laboratory, United States under Cooperative Agreement No. W911NF-20-2-0175. This work was also supported by Army ERDC Grant No. 1990749.

Data Availability Data supporting the findings of this study are availible from the corresponding author upon reasonable request.

Declarations

Competing Interests The authors declare no competing interests.

Ethical Approval Not applicable.

References

1. Tumkur, T.U., Voisin, T., Shi, R., Depond, P.J., Roehling, T.T., Wu, S., Crumb, M.F., Roehling, J.D., Guss, G., Khairallah, S.A., Matthews, M.J.: Nondiffractive beam shaping for enhanced optothermal control in metal additive manufacturing. Sci. Adv. **7**(38), eabg9358 (2021)
2. Shi, R., Khairallah, S.A., Roehling, T.T., Heo, T.W., McKeown, J.T., Matthews, M.J.: Microstructural control in metal laser powder bed fusion additive manufacturing using laser beam shaping strategy. Acta Mater. **184**, 284–305 (2020)
3. Bi, J., Wu, L., Li, S., Yang, Z., Jia, X., Starostenkov, M.D., Dong, G.: Beam shaping technology and its application in metal laser additive manufacturing: A review. J. Market. Res. **26**, 4606–4628 (2023)
4. Grünewald, J., Gehringer, F., Schmöller, M., Wudy, K.: Influence of ring-shaped beam profiles on process stability and productivity in laser-based powder bed fusion of AISI 316L. Metals **11**, 1989 (2021)
5. Wischeropp, T.M.: Advancement of Selective Laser Melting by Laser Beam Shaping. Springer, Light Engineering für die Praxis, Berlin, Heidelberg (2021)
6. Schmidt, M., Cvecek, K., Duflou, J., Vollertsen, F., Arnold, C., Matthews, M.: Dynamic beam shaping—Improving laser materials processing via feature synchronous energy coupling. CIRP Ann. **73**(2), 533–559 (2024)
7. Deisenroth, D., Weaver, J., Mekhontsev, S., Grantham, S., Moylan, S.P.: Laser Beam Metrology for AM-Bench 2022: Approaches, Results, and Lessons Learned. NIST,: Last Modified: 2025–04-01T21:04–04:00 Publisher: David Deisenroth, Jordan Weaver, Sergey Mekhontsev, Steven Grantham. Shawn P, Moylan (2025)
8. Roehling, T.T., Shi, R., Khairallah, S.A., Roehling, J.D., Guss, G.M., McKeown, J.T., Matthews, M.J.: Controlling grain nucleation and morphology by laser beam shaping in metal additive manufacturing. Mater. Des. **195**, 109071 (2020)
9. ISO 11146-2:2021(en), Lasers and laser-related equipment — Test methods for laser beam widths, divergence angles and beam propagation ratios — Part 2: General astigmatic beams
10. Qu, M., Guo, Q., Escano, L.I., Nabaa, A., Hojjatzadeh, S.M.H., Young, Z.A., Chen, L.: Controlling process instability for defect lean metal additive manufacturing. Nat. Commun. **13**, 1079 (2022)
11. Sow, M.C., De Terris, T., Castelnau, O., Hamouche, Z., Coste, F., Fabbro, R., Peyre, P.: Influence of beam diameter on Laser Powder Bed Fusion (L-PBF) process. Addit. Manuf. **36**, 101532 (2020)
12. Jardon, Z., Ertveldt, J., Hinderdael, M., Guillaume, P.: Process parameter study for enhancement of directed energy deposition powder efficiency based on single-track geometry evaluation. J. Laser Appl. **33**, 042023 (2021)
13. Kong, Y., Zhao, L., Zhu, L., Huang, H.: The selection of laser beam diameter in directed energy deposition of austenitic stainless steel: A comprehensive assessment. Addit. Manuf. **52**, 102646 (2022)
14. Weaver, J.S., Heigel, J.C., Lane, B.M.: Laser spot size and scaling laws for laser beam additive manufacturing. J. Manuf. Process. **73**, 26–39 (2022)
15. Bahador, A., Hamzah, E., Kondoh, K., Abubakar, T., Yusof, F., Saud, S.N., Ibrahim, M.K., Ezazi, M.A.: Defocusing effects of laser beam on the weldability of powder metallurgy Ti-based shape memory alloys. Procedia Engineering **184**, 205–213 (2017)
16. Metelkova, J., Kinds, Y., Kempen, K., de Formanoir, C., Witvrouw, A., Van Hooreweder, B.: On the influence of laser defocusing in Selective Laser Melting of 316L. Addit. Manuf. **23**, 161–169 (2018)
17. Li, W., Xu, L., Fu, Y., Tan, H., Jia, X., Li, K., Zhang, L., Wang, C., Duan, J.: Femtosecond laser welding of non-optical-contact ceramic and fused silica. Opt. Lett. **51**, 532–535 (2026)
18. Jia, X., Chen, Y., Yi, Z., Lin, J., Luo, J., Li, K., Wang, C., Duan, J., Polyakov, D.S., Veiko, V.P.: Tailoring sapphire-invar welds using burst femtosecond laser. Light: Adv. Manuf. **7**, 111–127 (2026)
19. Ding, Y., Wang, C., Jia, X., Liu, L., Gao, Z., Jiang, X., Wang, S., Yan, D., Lin, N., Li, Z., Duan, J.: Laser-optical-field-modulation fabricating large-aperture dual-band antireflection windows for MWIR and LWIR imaging. Int. J. Extreme Manuf. **8**, 025004 (2025)
20. Li, Z., Xu, J., Chen, Y., Li, K., Zhang, L., Jia, X., Wang, C., Duan, J.: Filament-assisted combined pulse laser ablation of metal targets: Mechanistic insights, efficiency enhancement, and spatial tolerance. J. Manuf. Process. **160**, 371–388 (2026)
21. Guo, C., Li, K., Liu, Z., Chen, Y., Xu, J., Li, Z., Cui, W., Song, C., Wang, C., Jia, X., Duan, J., Han, K.: CW laser damage of ceramics induced by air filament. Opto-Electron. Adv. **8**, 240296–13 (2025)
22. ISO 13694:2018 Optics and photonics — Lasers and laser-related equipment — Test methods for laser beam power (energy) density distribution, (2018)

23. Schmidt, A.J.: Optical characterization of thermal transport from the nanoscale to the macroscale. Thesis, Massachusetts Institute of Technology, (2008). Accepted: 2009-03-16T19:44:32Z
24. Bonnett Del Alamo, M., Soncco, C., Helaconde, R., BazoAlba, J.L., Gago, A.M.: Laser spot measurement using simple devices. AIP Adv. **11**, 075016 (2021)
25. Hossain, M.A., Canning, J., Cook, K., Jamalipour, A.: Smartphone laser beam spatial profiler. Opt. Lett. **40**(22), 5156–5159 (2015)
26. Edmund Optics.: Edmund optics beam profiler 4M. Product sheet
27. Kirkham, K., Roundy, C.: Current technology of beam profile measurement. In: Laser Beam Shaping, pp. 463–524, Boca Raton, FL: CRC Press, (2014)
28. Kaplan, A.F.H.: Analysis and modeling of a high-power Yb:fiber laser beam profile. Opt. Eng. **50**, 054201 (2011)
29. McClements, D., Zidonis, A.: Laser beam profiler: Definition, how it works, and purpose. Xometry Resources, (2026). Webpage
30. Deisenroth, D., Mekhontsev, S., Weaver, J., Webster, S.: Laser power density distribution metrology to support emerging trends in metal Additive Manufacturing. Procedia CIRP **124**, 741–745 (2024)
31. Deisenroth, D., Mekhontsev, S., Grantham, S.: Design and calibration of the fundamentals of laser-matter interaction (FLaMI) powder bed fusion testbed at the national institute of standards and technology. NIST, (2025)
32. 80 x 80mm Opal Checkerboard Target | Edmund Optics. Product sheet
33. Li, Q., Lee, B.-J., Zhang, Z.M., Allen, D.W.: Light scattering of semitransparent sintered polytetrafluoroethylene films. J. Biomed. Opt. **13**, 054064 (2008)
34. Weidner, V.R., Hsia, J.J.: Reflection properties of pressed polytetrafluoroethylene powder. JOSA **71**, 856–861 (1981)
35. Waldwick, B., Chase, C., Chang, B.Y.: Increased efficiency and performance in laser pump chambers through use of diffuse highly reflective materials. Laser Beam Shaping VIII **6663**, 202–208 (2007)
36. Hayakawa, S., Chono, T., Watanabe, K., Kawano, S., Nakamura, K., Miyazaki, K.: Ab initio calculation for electronic structure and optical property of tungsten carbide in a TiCN-based cermet for solar thermal applications. Sci. Rep. **13**, 9407 (2023)
37. Touloukian, Y.S., DeWitt, D.P.: Thermophysical properties of matter - the TPRC data series. Volume 7. Thermal radiative properties - metallic elements and alloys. (Reannouncement). Data book. Tech. Rep. AD-A-951941/4/XAB, Purdue Univ., Lafayette, IN (United States). Thermophysical and Electronic Properties Information Center, (1970)
38. Thorlabs unmounted N-BK7 Ground Glass Diffusers. Product sheet
39. Thorlabs · UV fused silica ground glass diffusers. Product sheet
40. Weidner, V.R., Hsia, J.J., Adams, B.: Laboratory intercomparison study of pressed polytetrafluoroethylene powder reflectance standards. Appl. Opt. **24**, 2225–2230 (1985)
41. Ylianttila, L., Schreder, J.: Temperature effects of PTFE diffusers. Opt. Mater. **27**(12), 1811–1814 (2005)
42. Blumm, J., Lindemann, A., Meyer, M., Strasser, C.: Characterization of PTFE using advanced thermal analysis techniques. Int. J. Thermophys. **31**, 1919–1927 (2010)
43. Yang, P., Zhang, Z.M.: Bidirectional reflection of semitransparent polytetrafluoroethylene (PTFE) sheets on a silver film. Int. J. Heat Mass Transf. **148**, 118992 (2020)
44. Thorlabs.: Thorlabs unmounted absorptive neutral density filters. Product sheet
45. SCHOTT North America, Inc.: Technical Information - Thermal loads on optical glass. Datasheet
46. Schröder, S., Kamprath, M., Duparré, A., Tünnermann, A., Kühn, B., Klett, U.: Bulk scattering properties of synthetic fused silica at 193 nm. Opt. Express **14**, 10537–10549 (2006)
47. Welsh, L.P., Tuchman, J.A., Herman, I.P.: The importance of thermal stresses and strains induced in laser processing with focused Gaussian beams. J. Appl. Phys. **64**, 6274–6286 (1988)
48. FLIR 04S2M EMVA 1288 imaging performance. Product sheet
49. INFINITY PHOTO-OPTICAL COMPANY.: Model K2 DistaMax™ long-distance microscope system. Product sheet
50. Myers, A.J., Quirarte, G., Ogoke, F., Lane, B.M., Uddin, S.Z., Farimani, A.B., Beuth, J.L., Malen, J.A.: High-resolution melt pool thermal imaging for metals additive manufacturing using the two-color method with a color camera. Addit. Manuf. **73**, 103663 (2023)